

PAPER • OPEN ACCESS

## Toroidal Alfvén eigenmode stability in JET internal transport barrier afterglow experiments










To cite this article: M. Fitzgerald *et al* 2022 *Nucl. Fusion* **62** 106001

View the [article online](#) for updates and enhancements.

You may also like

- [Scenario development for the observation of alpha-driven instabilities in JET DT plasmas](#)  
R. J. Dumont, J. Mailloux, V. Aslanyan et al.
- [TAE stability calculations compared to TAE antenna results in JET](#)  
F. Nabais, V. Aslanyan, D. Borba et al.
- [Robertson-Schrödinger formulation of Ozawa's uncertainty principle](#)  
Catarina Bastos, Alex E Bernardini, Orfeu Bertolami et al.

# Toroidal Alfvén eigenmode stability in JET internal transport barrier afterglow experiments

M. Fitzgerald<sup>1,\*</sup>, S.E. Sharapov<sup>1</sup> , P. Siren<sup>2</sup>, E. Tholerus<sup>1</sup> , M. Dreval<sup>3</sup> , G. Szepesi<sup>1</sup>, P. Vallejos<sup>4</sup> , T. Johnson<sup>4</sup> , N. Fil<sup>1</sup>, J. Ferreira<sup>5</sup>, P. Rodrigues<sup>5</sup> , A. Figueiredo<sup>5</sup> , D. Borba<sup>5</sup>, R. Coelho<sup>5</sup>, F. Nabais<sup>5</sup> , J. Mailloux<sup>1</sup>, H.J.C. Oliver<sup>1</sup>, C. Di Troia<sup>6</sup>, F. Napoli<sup>6</sup>, Ž. Štancar<sup>7</sup>, R. Dumont<sup>8</sup> , D. Keeling<sup>1</sup> and JET Contributors<sup>a</sup>

<sup>1</sup> CCFE, Culham Science Centre, Abingdon OX14 3DB, United Kingdom of Great Britain and Northern Ireland

<sup>2</sup> Department of Physics, University of Helsinki, 00014 Helsinki, Finland

<sup>3</sup> National Science Centre ‘Kharkiv Institute of Physics and Technology’, Institute of Plasma Physics, Kharkiv, Ukraine

<sup>4</sup> Fusion Plasma Physics, EES, KTH, SE-10044 Stockholm, Sweden

<sup>5</sup> Instituto de Plasmas e Fusão Nuclear, Instituto Superior Técnico, Universidade de Lisboa, Portugal

<sup>6</sup> ENEA, Fusion and Nuclear Safety Department, C.R. Frascati, Via E. Fermi 45, 00044 Frascati (Roma), Italy

<sup>7</sup> Jožef Stefan Institute, Ljubljana, Slovenia

<sup>8</sup> CEA, IRFM, F-13108 Saint Paul Lez Durance, France

E-mail: [Michael.Fitzgerald@ukaea.uk](mailto:Michael.Fitzgerald@ukaea.uk)

Received 9 May 2022, revised 30 June 2022

Accepted for publication 28 July 2022

Published 19 August 2022



CrossMark

## Abstract

In this work, we use reduced and perturbative models to examine the stability of toroidal Alfvén eigenmodes (TAEs) during the internal transport barrier (ITB) afterglow in JET experiments designed for the observation of alpha driven TAEs. We demonstrate that in JET-like conditions, it is sufficient to use an incompressible cold plasma model for the TAE to reproduce the experimental adiabatic features such as frequency and position. When ion cyclotron resonant heating (ICRH) is used to destabilize TAEs, the core-localised modes that are predicted to be most strongly driven by minority ICRH fast ions correspond to the modes observed in the DD experiments, and conversely, modes that are predicted to not be driven are not observed. Linear damping rates due to a variety of mechanisms acting during the afterglow are calculated, with important contributions coming from the neutral beam and radiative damping. For DT equivalent extrapolations of discharges without ICRH heating, we find that for the majority of modes, alpha drive is not sufficient to overcome radiative damping.

\* Author to whom any correspondence should be addressed.

<sup>a</sup> See Joffrin *et al* 2019 (<https://doi.org/10.1088/1741-4326/ab2276>) for the JET Contributors.



Original content from this work may be used under the terms of the [Creative Commons Attribution 4.0 licence](https://creativecommons.org/licenses/by/4.0/). Any further distribution of this work must maintain attribution to the author(s) and the title of the work, journal citation and DOI.

Keywords: JET, D–T, TAE, alpha, ITB, afterglow, stability

(Some figures may appear in colour only in the online journal)

## 1. Introduction

A great deal of effort and interest has been devoted to demonstrating the possible excitation of Alfvénic instabilities by super-Alfvénic fusion products, particularly alpha particles, a phenomenon that is important to understand and control in future burning plasmas [1]. Recent work on JET [2] has been focussed on creating the conditions for unambiguous observation of alpha driven toroidal Alfvén eigenmodes (TAEs) by exploiting the long slowing down time of alpha particles and the more rapid thermalisation of beam ions, supporting some existing evidence from JET [3] and TFTR [4]. Afterglow scenarios were designed to achieve a transient maximum performance to generate a large driving fusion alpha population, followed by rapid removal of neutral beam heating to minimize damping effects. Deuterium experiments were conducted to establish high performance internal transport barrier (ITB) scenarios at elevated safety factor with a view that they could be repeated in DT. Although generally omitting ICRH to avoid creating another fast particle population, some of these experiments deliberately employed ICRH during the afterglow to probe the stability of TAEs, allowing the validation of stability calculations.

In this work, we test the quantitative predictive capability of reduced and perturbative models for TAE stability in a particular JET ITB scenario when supplied by approximate inputs from the available integrated modelling data.

Experimental features reproduced by this workflow include:

- Location of rational surfaces
- Mode frequency
- Mode position
- Strongest driven modes
- Modes that are absent
- Time of onset during afterglow

After demonstrating capabilities in reproducing experimental features in pure deuterium plasma, we present an extrapolation to 50:50 deuterium–tritium plasmas to assess the likelihood of alpha driven TAEs being excited.

## 2. Theory

Tokamak plasmas are known to support a broad range of wave phenomena propagating at different characteristic speeds. The local wave dispersion relation includes the Alfvén continuum  $\omega^2 \approx k_{\parallel}^2 V_A^2$  and ion-sound continuum  $\omega^2 \approx k_{\parallel}^2 c_s^2$ , with  $V_A$  and  $c_s$  denoting respectively the Alfvén and ion-sound speeds. The squared ratio of  $c_s$  and  $V_A$  depends on  $\beta$ , the ratio of magnetic to thermal pressure. In a conventional tokamak such as JET,

these speeds are well-separated and Alfvén waves can be identified that are dominated by the interplay between magnetic field tension and plasma inertia, rather than plasma compression. For reactor-relevant conditions, these waves must be kept as small oscillations around an equilibrium with  $\frac{\delta B}{B} \ll 1\%$ . The toroidally symmetric equilibrium magnetic field balances the pressure of a mostly isotropic plasma as expressed in the fluid picture with the Grad–Shafranov equation

$$R^2 \nabla \cdot \left( \frac{\nabla \psi}{R^2} \right) = -R \mu_0 J_{\phi}(R, \psi) \quad (1)$$

$$J_{\phi}(R, \psi) = R p'(\psi) + f f'(\psi) / \mu_0 R$$

where the poloidal flux functions correspond to the pressure force  $-\nabla p = -p'(\psi) \nabla \psi$  and the covariant toroidal magnetic field  $R B_{\phi} = f(\psi)$ . In the kinetic picture on collisionless timescales, a particle distribution function is in equilibrium if and only if it can be written in terms of particle orbit constants of motion

$$F = F(E, \mu, P_{\phi}; \sigma) \quad (2)$$

for energy  $E$ , magnetic moment  $\mu = \frac{\frac{1}{2} m v_{\perp}^2}{B} + O\left(\frac{\rho}{L}\right)$ , toroidal canonical momentum  $P_{\phi} = m R v_{\phi} + Z e \psi$  and  $\sigma \equiv \text{sign}(v_{\parallel})$ . The above expressions correspond to sign conventions [5] where poloidal flux relates to field by  $\mathbf{B}_p \equiv \nabla \psi \times \nabla \phi$  and toroidal direction obeys  $\hat{R} \times \hat{\phi} = \hat{Z}$ .

The two pictures, represented by equations (1) and (2), are reconciled for the majority thermal plasma with zero orbit width where  $F = F(E, \psi)$ . The fast particle distributions associated with NBI, ICRH or the fusion products cannot be said to satisfy this assumption in JET-like conditions; NBI and ICRH orbits can exhibit strong directionality favouring a given on-axis pitch  $\Lambda \equiv \frac{\mu B_0}{E}$  and all fast particles exhibit a finite orbit width through  $P_{\phi}$ . Although these quantities feature naturally in the kinetic theory, integrated modelling focusing on flux-surface average quantities tends to ignore these effects for computational convenience with varying levels of justification in current tokamaks. As an example: for large aspect ratio, a fast pressure approximation [6] is justified to capture the fast particle forces in the Grad–Shafranov equation.

The TAE was first identified [7] as a class of discrete oscillatory solution to the linearized ideal MHD equations in the limit of small  $\beta$ . These global eigenmodes exist within the TAE gap of the Alfvén continuum at angular frequencies close to

$$\omega_{\text{TAE}} = \frac{V_A}{2qR}. \quad (3)$$

These incompressible ideal solutions from the fluid theory may also be found in the kinetic theory when solving for the ‘adiabatic’ terms in the linearized gyrokinetic equation, or by

assuming a cold plasma dispersion relation for the given field and density. Real and imaginary corrections to the TAE eigenfrequency and mode structure come from non-ideal effects such as resonant wave–particle interaction, collisions, finite orbit width and finite Larmor radius [8, 9]. When these effects are weak, they provide only drive, damping and frequency corrections to what are in essence ideal MHD solutions, inviting a perturbative approach.

Resonant wave–particle interaction is computed perturbatively with linear codes such as CASTOR-K [10] and NOVA-K [11], and nonlinear codes such as HAGIS [12] and HALO [13]. These perturbative calculations require inputs of the ideal eigenmodes from linear MHD codes such as MISHKA-1 [14] and CASTOR [15].

The further non-ideal contributions from finite Larmor radius and parallel electric field lead to the coupling of shear waves with kinetic Alfvén waves with a combined local dispersion relation

$$\omega^2 = k_{\parallel}^2 V_A^2 \left[ 1 + k_{\perp}^2 \rho_i^2 \left( \frac{3}{4} + \frac{T_e}{T_i} (1 - i\delta(\nu_e)) \right) \right] \quad (4)$$

with ion Larmor radius  $\rho_i = (m_i T_i)^{1/2} / eB$  and collisional dissipation  $\delta(\nu_e)$ , and a corresponding modification to the global TAE wave equation. The collisional dissipation captures the passing electron resistive losses and can be computed from the collision frequency  $\nu_e$  with trapped electrons.

The modified kinetic TAE wave equation resembles the resistive MHD equations but with a complex number substituting for conventional resistivity, allowing non-perturbative computation of some nonideal effects in CASTOR [9]. The coupling between kinetic Alfvén waves and TAEs leads to radiative damping of TAEs when their frequencies lie below the TAE gap frequency equation (3) [16]. Full non-perturbative calculations can also be performed using gyrokinetic or hybrid codes [17–19] which attempt to solve for all ideal and non-ideal effects simultaneously, including the difficult to resolve resonant wave–particle interaction. For slowly growing/decaying modes, power transfer between waves and particles occurs for a small fraction of particles satisfying the resonance condition [20]

$$0 = n \langle \omega_{\phi} \rangle + p \omega_{\theta} - \omega \quad (5)$$

where  $n$  is the wave toroidal mode number,  $\langle \omega_{\phi} \rangle$  and  $\omega_{\theta}$  are the bounce-averaged  $\langle \cdot \rangle$  toroidal and poloidal frequencies of the particles, and  $p$  is an integer that labels each Fourier component in the time varying power transfer. For deeply passing particles and small orbit width, the strongest Fourier component occurs when  $p \approx m$  the poloidal mode number for one of the eigenmode harmonics, corresponding to when  $\omega \approx \mathbf{k} \cdot \mathbf{v}$  for that Fourier component. Analytical expressions [21] of alpha drive and ion Landau damping for of TAEs have been derived for this lowest order power transfer corresponding to the conditions  $v_{\parallel} = V_A$  and  $v_{\parallel} = V_A/3$ . More generally, the linear growth rate  $\gamma_L$  depends on the distribution function gradients at resonance

$$\gamma_L = \int d^3x d^3v \sum_{\sigma} \sum_p \frac{\delta\gamma(x, v; p, \sigma)}{n \langle \omega_{\phi} \rangle + p \omega_{\theta} - \omega} \quad (6)$$

$$\delta\gamma(x, v; p, \sigma) \propto \omega \left( \frac{\partial F}{\partial E} \right)_{\mu, P_{\phi}} - n \left( \frac{\partial F}{\partial P_{\phi}} \right)_{E, \mu}$$

On JET [22], resonant wave–particle interaction with TAEs occurs between ICRH, NBI, fusion products and thermal plasma species. For typical JET magnetic fields and densities, the ion velocities present in the NBI and thermal distributions fall below  $V_A$  and do not contribute drive to TAEs. Drive of TAEs observed on JET is almost exclusively provided by ICRH.

In the sections that follow, we compare predictions of this stability theory to experimental data on an existing DD discharge 92416 during the afterglow, and provide extrapolations of TAE stability in DT for the best performing scenario, which was achieved in discharge 96852.

### 3. Predictions for the JET ITB afterglow

#### 3.1. Overview of the JET ITB afterglow

Recent scenario development of JET ITBs has been described previously [2, 23], but here we give a brief summary of key features of shots 92416 and 96852. The plasma is a monotonic  $q(\psi)$  low shear discharge with  $B_{\text{vac}} = 3.4$  T and  $I_p = 2.5$  MA operating at elevated  $q_0 > 1.5$ . The pulses are majority deuterium with measured edge hydrogen concentration  $n_H/n_e \sim 2\%–7\%$ . NBI heating exceeding approximately 25 MW for JET with the ITER-like (metal) wall can lead to the formation of an ITB at the  $q = 2$  surface, with some sensitivity on timing and density, the latter being set as low as shine-through limits allow. Strong density and ion temperature peaking are a feature of this scenario which can result in ion/electron temperature ratios of order  $T_i \approx 2T_e$  when discharges are successful at producing an ITB. Figure 1 gives the measured magnetic probe signal at the expected TAE gap frequency before and after the full NBI power phase during 92416. Three modes are observed at 6.2 s with toroidal mode numbers  $n = 4, 5, 6$ . These modes occur during a period when the NBI has been stopped and the plasma is cooling. For 92416, ICRH is maintained during the afterglow so as to deliberately destabilize TAEs. A higher performance version of the same shot has been developed to be repeated in DT, 96852, with no ICRH and peak transient neutron rate  $R_{\text{NT}} = 2.45 \times 10^{16}$ . A range of similar pulses were developed with very good reproducibility in  $q$ -profiles [2], with variation in performance owing to small changes in NBI waveform and gas puff affecting the appearance of the transport barrier.

#### 3.2. Fluid equilibrium reconstruction

The linear TAE spectrum depends sensitively on the equilibrium, particularly on the  $q$ -profile. Inference of equilibrium is provided on JET using the EFIT code [24]. However, during the afterglow MSE measurements are unavailable. A large variation in  $q$ -profiles between equally valid EFIT solutions

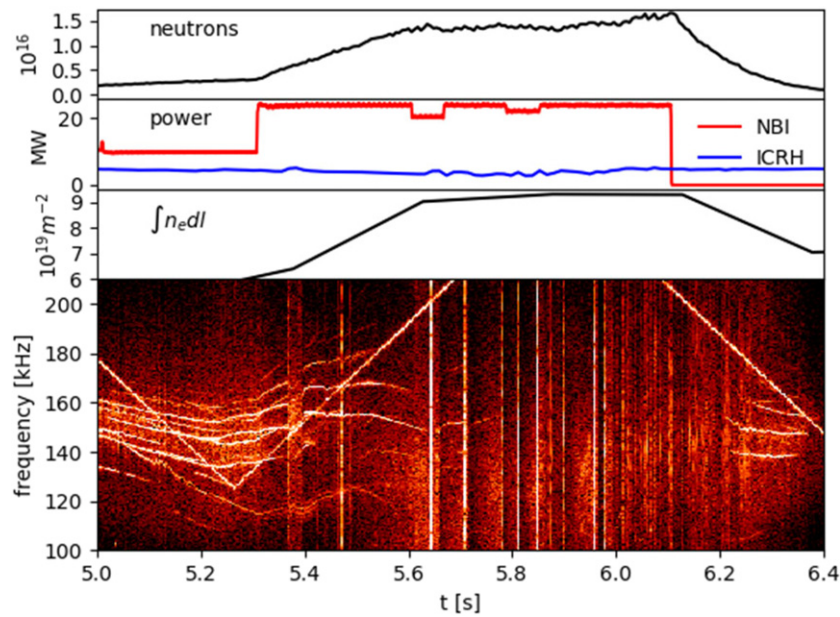


Figure 1. JET shot 92416 afterglow scenario details (above) magnetic spectrum (below).

is possible if internal current profile constraints are absent [25]. Considering both free functions in the Grad–Shafranov equation (equation (1)), detailed information on  $p'(\psi)$  is available via measurements and fast ion modelling, but very little is available to constrain  $ff'(\psi)$  without MSE or computed parallel current constraint. Over-fitting the pressure pedestal in these ITB cases led to implausibly low safety factor in the core. For this study, both free flux functions  $p'(\psi)$  and  $ff'(\psi)$  were instead parametrised by simple quadratic polynomials, and experimental thermal pressure and computed fast pressure from TRANSP [26] were used as input constraints. Although it is likely that this approach does not capture equilibrium features in the pedestal, our focus was to faithfully capture the core  $q$ -profile.

MHD spectroscopy was used to validate this procedure for our ITB cases of interest. The locations of instabilities, likely to be tearing modes, were identified using cross-correlation between electron cyclotron emission and Mirnov coil data, and toroidal mode numbers were obtained from the toroidal separation of the Mirnov array [27]. Two modes, with  $n = 2$  and  $n = 3$ , were identified at different times. This provided measurements of the  $q = 2$  surface at major radius  $R = 3.15 \pm 0.05$  m and  $q = \frac{2}{3}$  at  $R = 3.45 \pm 0.05$  m at times 5.52 s and 5.69 s respectively, before the time of interest 6.2 s. A comparison with the reconstruction is presented in figure 2.

At highest performance, the reconstructed position of the  $q = 2$  surface also agrees with the position of the ITB; an integer value always appears to be necessary for JET ITBs with monotonic shear [28]. A steady decay from  $q_{\min} = 2$  to  $q_{\min} = 1$  can also be inferred from Alfvén cascades after the time of interest, beginning from 6.5 s. In practice, the location and timing of the appearance of the  $q = 2$  surface was a robust and reproducible experimental feature between pulses, giving confidence of similar  $q$ -profile evolution for

many shots differing in NBI waveform and also regardless of whether ICRH heating was incorporated.

### 3.3. Incompressible linear stability

Magnetics signals close to the TAE gap frequency computed with equation (3) were observed both before the time of peak performance and during the afterglow (figure 1). A reconstructed equilibrium at the time of appearance during the afterglow was obtained at 6.2 s and metric elements of the straight field line coordinates were obtained with HELENA [29] for input to linear MHD calculations.

As mentioned previously, the three experimentally observed modes had toroidal mode numbers  $n = 4, 5, 6$ . On JET, the convention for positive toroidal mode number and mode frequency indicates a mode propagating in the ion-diamagnetic direction for peaked core pressure, which corresponds to a toroidal wave number  $n\nabla\xi$  using the  $\hat{R} \times \hat{Z} = \hat{\xi}$  sign convention. Plasma current, toroidal field, toroidal rotation and neutral beams are all in the same toroidal direction as the propagating modes.

The straight field line metric elements from HELENA [29] and a normalized mass density profile were used as inputs for the incompressible linear MHD code MISHKA-1 [14]. The mass density was approximated on the assumption of 100% deuterium with number density from fitted experimental LIDAR and Thompson scattering electron number density data. A range of TAE eigenmode solutions were found for the toroidal mode numbers  $n = 4, 5, 6$ . The rotation of the plasma at the location of the observed modes was estimated as the difference in frequency for adjacent mode numbers, owing to the expected Doppler shift  $\omega_{\text{lab}} = \omega_{\text{plasma}} + n\Omega$  giving a rotational frequency at the modes of  $\Omega/2\pi = 10$  kHz, assuming the modes are in similar location with similar rotation. Charge-exchange recombination spectroscopy (CXRS) measurements



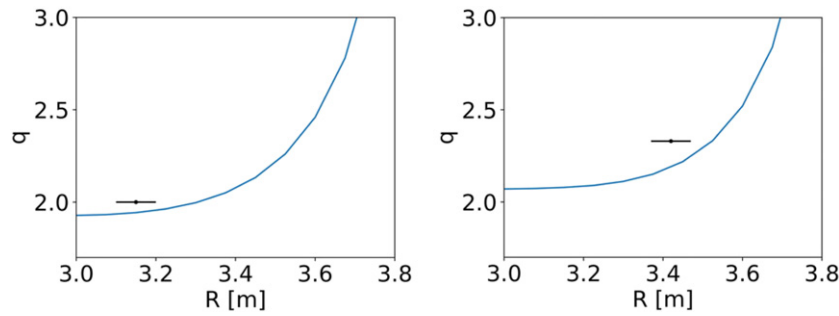


**Figure 2.** Comparison of  $q$ -profile of EFIT reconstruction (curves) to measured midplane position (point with errorbar) of tearing modes at 5.52 s (left) and 5.69 s (right) in JET shot 92416. These correspond to rational surfaces  $q = 2$  and  $q = 7/3$ .

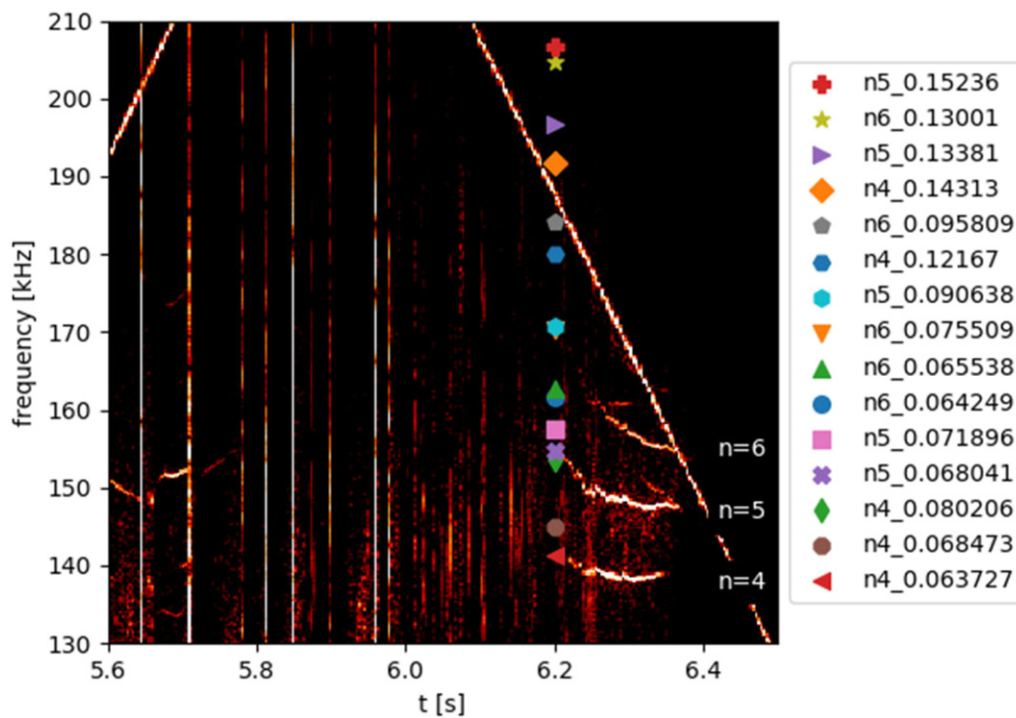


**Figure 3.** JET shot 92416 magnetic spectrum with MISHKA-1 TAE solutions overlaid. All frequencies are given in the lab frame assuming a toroidal rotation of 10 kHz. Modes are coloured by toroidal mode number and labelled with their normalized eigenvalue as ‘ $n\{\text{mode number}\}_{\omega/\omega_A}^2$ ’.

before the afterglow at 6.1 s range from 17 kHz at the magnetic axis to 10 kHz at a midplane location of  $R = 3.47$  m. Although charge exchange measurements were not available during the afterglow, x-ray crystal spectroscopy (XCS) Doppler measurements fall by 25%, which if replicated in the whole profile, would suggest 10 kHz rotation occurs at 3.4 m at time of TAE observation.

The range of eigenmodes predicted from the incompressible theory for the measured profiles and assumed rotation in the lab frame occurred in the frequency range 135–165 kHz. Solutions in this range of frequencies have been overlaid onto the measured magnetic spectrum in figure 3. Once toroidal mode number is accounted for, three predicted solutions are found that correspond to within 2%–3% of the observed signals. This supports the conclusion that the adiabatic properties of the modes are well modelled by TAEs from the

incompressible theory despite the presence of an ITB and ion temperature  $\sim 10$  keV.

The eigenmodes that most resemble experimental observations correspond with archetypal core-localised TAEs which are characteristic of low magnetic shear in the analytical theory [30] and found to be most unstable in ITER baseline calculations [31, 32]. These three modes are also of ‘ballooning’ type, where the frequencies are found within the lower half of the TAE gap in the Alfvén continuum, and the mode positions are weighted towards the outboard side of the midplane. The MHD prediction of the eigenmode is presented in figure 4 (top left) and figure 4 (top right) along with reflectometer measurements in figure 4 (bottom). The reflectometer measures density fluctuations at a given probed frequency. The TAEs observed on the magnetics correlate with density fluctuations, with the  $n = 4$  and  $n = 5$  mode frequencies evident in figure 4 (bottom).

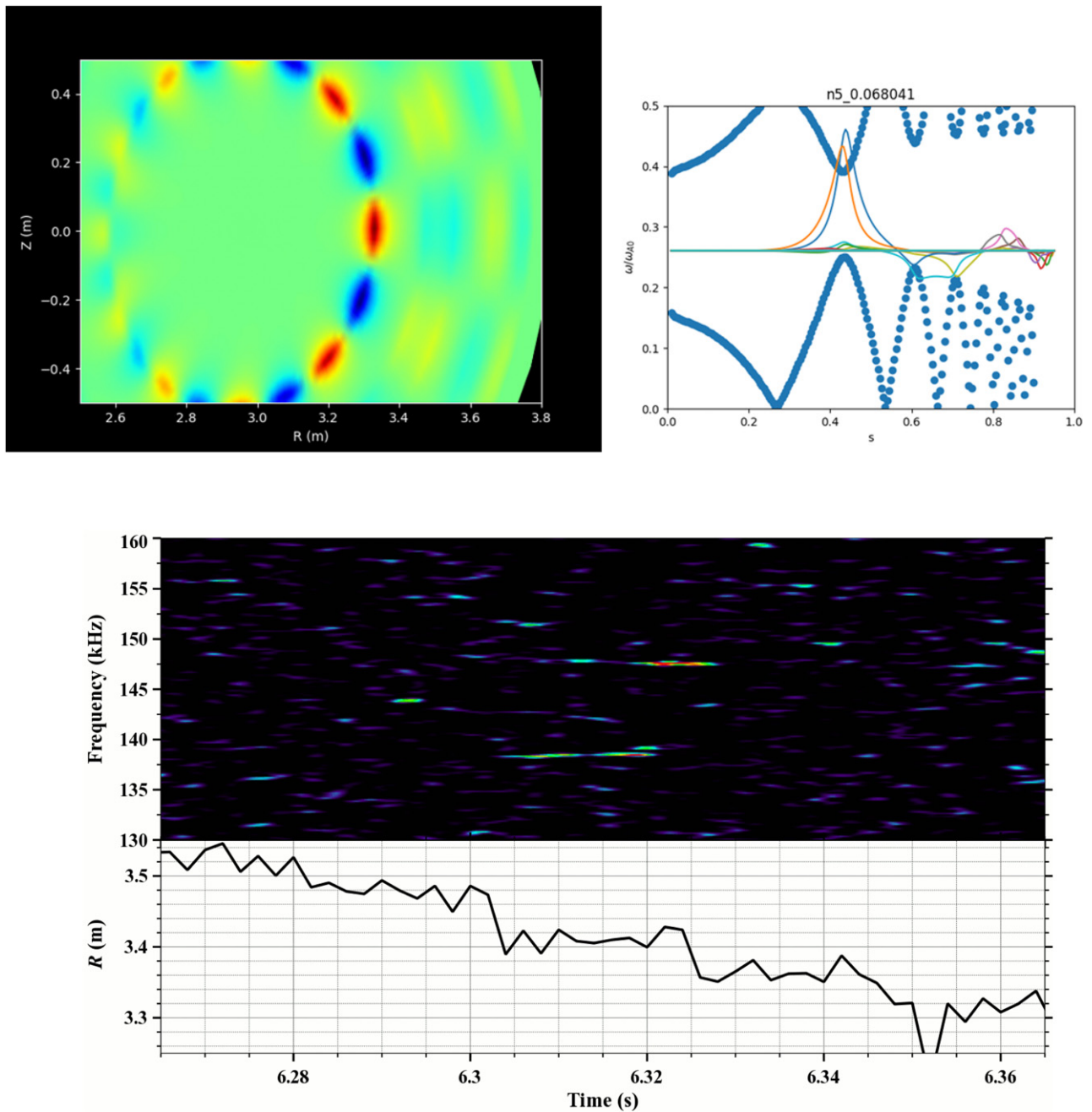


**Figure 4.** MISHKA-1 2D perturbed radial velocity  $sV^1$  where  $s = \sqrt{\psi_p}$  (top left) and the 1D equivalent superimposed on the Alfvén continuum (top right) for  $n = 5$  eigenmode observed initially at 150 kHz. Reflectometry measurements (bottom) give the position of the TAEs in JET shot 92416, with the mode at 147 kHz matching the  $n = 5$  mode found on magnetics at 6.325 s.

The probed frequency is scanned in time, altering the radial position where the density fluctuation is measured, depending on the cut-off in the probe wave local dispersion relation. The inferred radial position is shown below the spectrum. The  $n = 5$  is measured at an outboard major radius of  $R \approx 3.33$  m which is consistent with MISHKA-1 predictions. This is comparable with the 3.4 m estimate from rotation assumptions made earlier and CXRS/XCS Doppler measurements. It is interesting that the  $n = 4$  mode appears slightly earlier on reflectometry, but this shift of a few cm outwards is not present in the MISHKA-1 prediction for  $n4\_0.068473$ , although the

$n = 4$  mode is wider by a comparable amount. Another  $n = 4$  mode found,  $n4\_0.063727$  peaking at 3.4 m could perhaps be a better fit, but at this level of detail with eigenfrequency varying within 2%–3%, one would expect that accuracy in  $q$  profile reconstruction (figure 2) must also come into consideration before looking for additional physics.

#### 3.4. Kinetic ICRH minority and NBI equilibrium

Radio-frequency heating of a hydrogen minority was included in shot 92416 for the purpose of probing TAE stability during

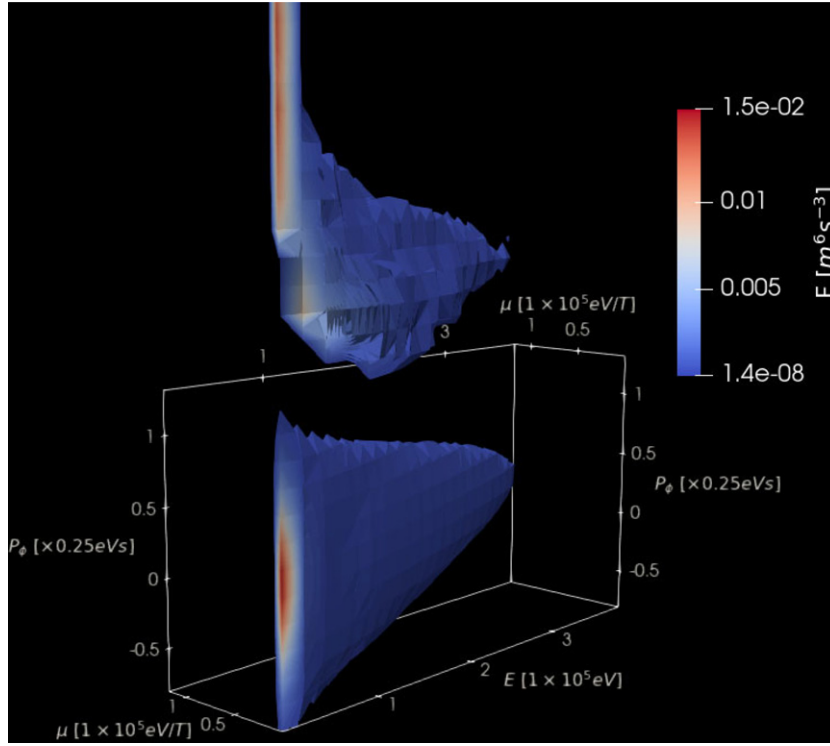


**Figure 5.** SELFO ICRH distribution function at 6.1 s (above) and analytical fitted form (below).

the afterglow. Calculations of resonant wave–particle TAE drive requires the input of the minority hydrogen distribution of the form expressed in equation (2) to capture effects of finite orbit width and strong anisotropy. The SELFO code [33] was used to solve the quasilinear equations for the ICRH fast proton distribution in constants of motion. Additionally, NBI heating was present during the high-performance phase, and then turned off to decrease resonant wave–particle TAE damping. The ASCOT code [34] was used to solve the Fokker–Plank equation for the fast deuterons in position and velocity coordinates, and then converted to the equilibrium form given by equation (2), capturing all finite orbit width and anisotropy features present in the beam distributions.

The output of distribution function modelling is presented in figures 5 and 6. Both distributions show significant anisotropy, particularly the SELFO distribution which is strongly peaked around  $\Lambda = \frac{\mu B_0}{E} = 1$  as expected from the quasilinear theory applied to on-axis minority heating.

Being Monte-Carlo solutions, the distributions feature significant Monte-Carlo noise, particularly along edges of the topological orbit boundaries that are sparsely populated in reality, and poorly resolved in computation. Although perfectly valid as collisionless equilibrium distribution functions by virtue of their representation  $F = F(E, \mu, P_\phi; \sigma)$ , they are not physically realisable because they violate a smoothness condition in the Fokker–Plank equation; drag and diffusion terms in the collision operators would become large around any sharp features in the equilibrium, immediately smoothing the distribution. Stability calculations using such unphysical equilibria would presumably produce numerically converged but physically irrelevant results if these gradients

happen to occur near the resonance condition. Under these circumstances, numerical convergence of the entire integrated stability calculation would require convergence of the derivatives of the 3D distribution function in the Monte-Carlo simulations.

In order to de-couple numerical convergence of heating codes from stability calculations while retaining finite orbit-width and anisotropic effects, physically motivated parametric distribution functions derived in [35, 36] were adopted

$$F_{\text{ICRH}}(E [\text{eV}], \mu [\text{eV T}^{-1}], P_\phi [\text{eV s}]) \equiv N \frac{(1.0 + \frac{\mu/E}{\lambda_0}) (\frac{E}{T})^\alpha}{\sqrt{2\pi}} E^{-\frac{3}{2}} e^{-\frac{(P_\phi - P_0)^2}{\Delta P^2}} \times e^{-\frac{E}{T} \left(1 + \frac{(\frac{\mu}{E} - \lambda_0)^2}{\Delta \lambda^2}\right)} \quad (7)$$

$$F_{\text{NBI}}(E [\text{eV}], \mu [\text{eV T}^{-1}], P_\phi [\text{eV s}]) \equiv N \frac{1}{\sqrt{2\pi}} \frac{1}{E^{\frac{3}{2}} + E_C^{\frac{3}{2}}} e^{-\frac{(P_\phi - P_0)^2}{\Delta P^2}} e^{-\frac{E}{T} \left(\frac{(\frac{\mu}{E} - \lambda_0)^2}{\Delta \lambda^2}\right)}. \quad (8)$$

The free parameters  $T, \lambda_0, \Delta \lambda, P_0, \Delta P, N, E_C, \alpha$  were manually fitted to best reproduce the functions  $\left(\frac{\partial F}{\partial E}\right)_{\mu, P_\phi}$  and  $\left(\frac{\partial F}{\partial P_\phi}\right)_{E, \mu}$  and the integral velocity moments of the distribution, the density and pressure. The parameters used are listed in table 1, with the resulting distributions plotted in figures 5 and 6. Even after this tedious procedure, the fitted ICRH distribution had missing outboard features in the density profile, and a



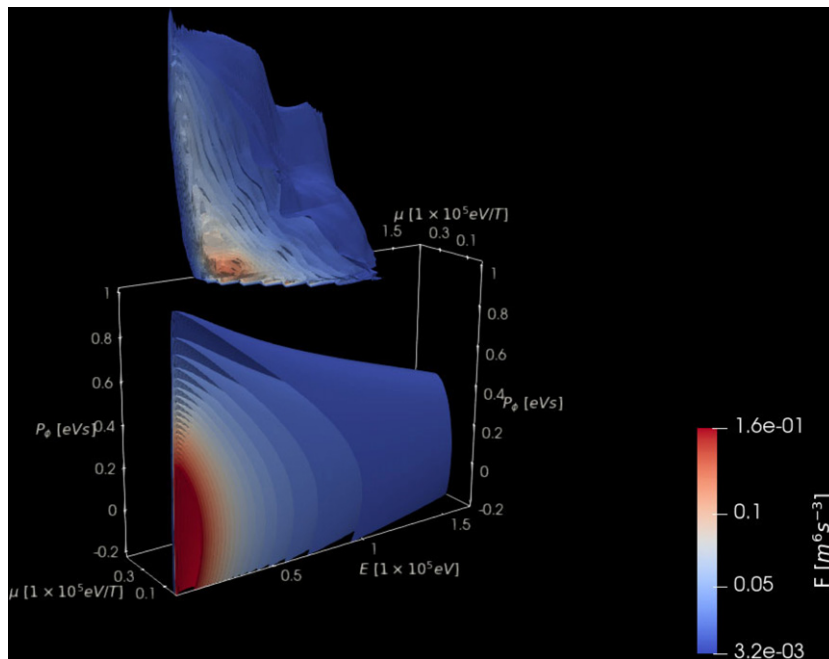


Figure 6. ASCOT NBI distribution function at 6.1 s (above) and analytical fitted form (below).

Table 1. Fitted parameters for analytical representation of heating code output, giving the distribution functions in S.I. units.

	$T(\text{eV})$	$\lambda_0(T^{-1})$	$\Delta\lambda(T^{-1})$	$P_0(\text{eV s})$	$\Delta P(\text{eV s})$	$E_c(\text{eV})$	$\alpha$	$N$
ICRH	30 000	0.3	0.05	0.07	0.229	—	0.8	$0.3 \times 10^6$
NBI $\sigma = +$	291 97.1	0.18	0.3	0.0	0.5525	25 000	0.0	$2.5 \times 10^6$
NBI $\sigma = -$	280 90.5	0.18	0.3	0.0	0.6744	25 000	0.0	$2.5 \times 10^6$

resulting fitted pressure that was 30% too high compared with SELFO outputs. No automatic tools were available to perform fits to ICRH/NBI Monte-Carlo output, systematically quantifying the fitting error and propagating implications. Moreover, as the analytical forms do not capture all processes modelled in Monte-Carlo heating codes, trade-off decisions are involved in which features of the distribution function are most important to capture. We deem this aspect of the integrated fast-ion stability modelling an important unsolved problem beyond the scope of this study.

### 3.5. Resonant ICRH linear stability

Full-orbit calculations of linear wave–particle interaction were made with HALO using the fitted ICRH distribution approximation, along with the equilibrium and incompressible eigenmodes from the presented EFIT/HELENA/MISHKA analysis. The resulting linear growth rates are presented in figure 7. Even before the consideration of damping mechanisms, some important experimental features are evident. Firstly, the three strongest linearly driven MISHKA-1 eigenmodes correspond exactly to those observed during the afterglow in figure 3, with

the most unstable of the three modes, the  $n = 5$ , appearing first, and the remaining two also appearing in order. Secondly, although most of the ICRH fast ion energy is localised in the core, the calculations correctly predict a very significant difference between inboard and outboard TAE stability for the core modes. This is due to the anisotropy of the fitted ICRH distribution function consisting of mainly trapped particles with banana tips along  $R = R_{\text{mag}}$ , with orbits that remain on the low field side. While MHD calculations predict the ‘anti-ballooning’ solutions near the top of the frequencies are possible, experimentally, the inboard TAEs are not evident in figure 3, with no modes observed above 170 kHz. This is despite inboard TAEs not being affected by radiative damping.

### 3.6. Linear drive and damping during the DD afterglow

A detailed examination of the core ballooning  $n = 5$  TAE observed during the DD afterglow was conducted to understand the strongest contributions to linear drive and damping. Smooth experimental fits of 1D electron and ion temperature were used for the calculation of bulk thermal plasma effects.

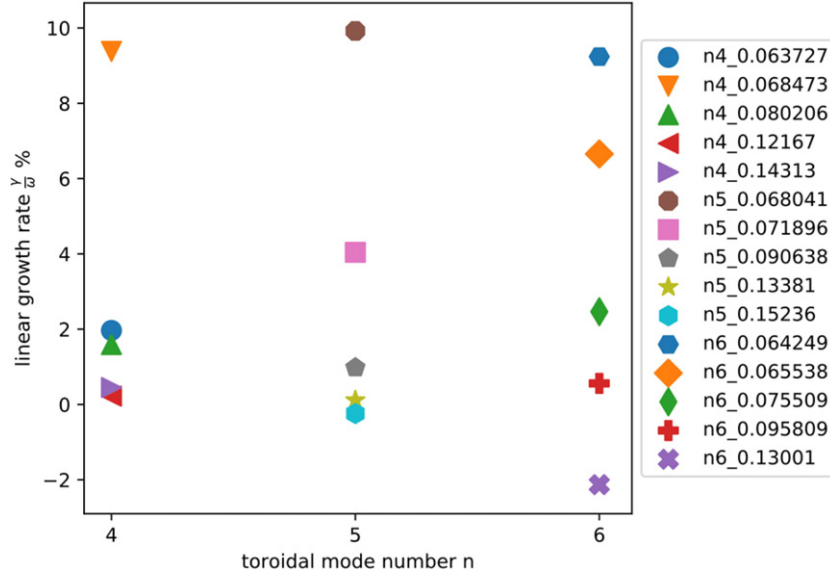


**Figure 7.** HALO wave–particle interaction calculations for the drive of incompressible TAEs by ICRH hydrogen minority ions. The three most unstable modes correspond well to three observed modes in the experimental spectra.

The HALO code was used for full-orbit perturbative calculations of ICRH drive, NBI damping and thermal ion Landau damping. CASTOR-K was used for drift-kinetic calculations of ion Landau damping. For non-perturbative calculations of damping, CASTOR was used to compute the radiative damping using the complex resistivity approximation, while both radiative damping and all other thermal plasma effects were computed with the linear gyrokinetic code LIGKA.

For the CASTOR complex resistivity calculation, values were taken at the position of the eigenmode:  $R_0 = 2.96$  m,  $R = 3.30$  m,  $T_i = 5.18$  keV,  $T_e = 3.40$  keV,  $q = 1.86$ ,  $|B| = 3.06$  T,  $|B_0| = 3.4$  T,  $n_e = 3.52 \times 10^{19}$  m $^{-3}$ ,  $n_{e0} = 4.93 \times 10^{19}$  m $^{-3}$ . The resistivity normalized to Alfvén frequency on axis  $\omega_A$  for CASTOR input [32] is given by

$$\begin{aligned} \omega_{\text{TAE}} &= \frac{V_A(R)}{2qR}, \omega_A = \frac{V_A(R_0)}{R_0} \\ \xi &= \frac{3}{4} + \frac{T_e}{T_i}(1 - i\delta) \\ \eta &= i\xi \left( \frac{\omega}{\omega_A} \right) \left( \frac{\omega}{\omega_{\text{TAE}}} \right)^2 \left( \frac{\rho_i}{R_0} \right)^2 \end{aligned} \quad (9)$$

giving  $\text{Im}\{\eta\} = 4.9 \times 10^{-7}$ . The inclusion of this imaginary component in the resistivity results in a combination of kinetic Alfvén wave and TAE in the CASTOR solution. Because the kinetic Alfvén wave is very sensitive to the wave dissipation  $\delta$ , increasing the dissipation suppresses the kinetic Alfvén wave, leaving only a damped TAE. Extrapolation of TAE damping to  $\delta = 0$  gives the inherent radiative damping of the TAE. The result of such a scanning process, shown in figure 8, leads to a radiative damping value of  $\frac{\gamma}{\omega} = -1\%$ .

Analytical approximations for ion Landau damping were also computed. Analytical theory of resonant wave–particle interaction with TAEs [21] assuming zero orbit width gives the following expression for damping due to a Maxwellian

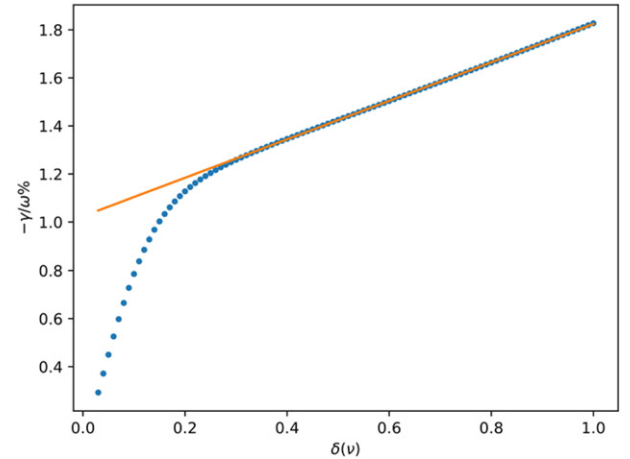


**Figure 8.** CASTOR scan of wave dissipation to obtain the radiative damping of the  $n = 5$  TAE mode of interest.

population

$$\begin{aligned} \frac{\gamma}{\omega} &= -q^2\beta \left[ g(\lambda) + g\left(\frac{\lambda}{3}\right) \right] \\ g(\lambda) &= \frac{\pi^{1/2}}{2} \lambda (1 + 2\lambda^2 + 2\lambda^4) e^{-\lambda^2} \\ \lambda &\equiv \frac{V_T}{V_A}, \quad V_T \equiv \sqrt{\frac{2T_i}{m}}, \quad \beta = 2\mu_0 n_i T_i / B^2 \end{aligned} \quad (10)$$

The analytical expression in equation (10) captures the lowest order TAE resonances  $v_{\parallel} = V_A$  and  $v_{\parallel} = V_A/3$  in the terms  $g(\lambda)$  and  $g(\frac{\lambda}{3})$  respectively.

A summary of linear findings during the afterglow are presented in figure 9. Damping from NBI and radiative damping are of similar order for these core localised modes at the beginning of the afterglow. Antenna measurements at later times in the pulse [23] seem to be fully explained by radiative

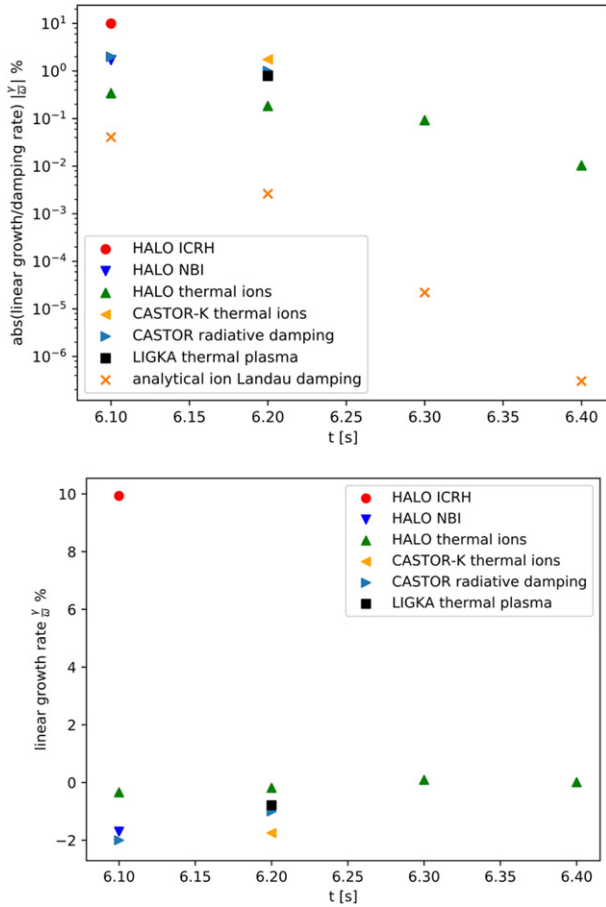


**Figure 9.** Summary of linear drive and damping findings during the afterglow. TAE appears at 6.2 s.

damping and do not suggest any further damping mechanisms not already mentioned. There is good agreement between the perturbative model HALO and the non-perturbative model LIGKA that ion Landau damping is small, although CASTOR-K predicts a large contribution from trapped particles. Both CASTOR and LIGKA agree that radiative damping by the bulk thermal plasma is responsible for damping the core TAEs when NBI fast ions are assumed absent.

Given that TAEs are suppressed at 6.1 s and only appear at 6.2 s, the ICRH drive calculations are clearly too high by at least a factor 2 compared with damping. The large error can be understood by examining the regions in particle phase space where the resonant wave–particle interaction is producing the largest power transfer. To illustrate, the HALO code was run for 30 wave periods with fixed wave amplitude  $\frac{\delta B}{B} = 1 \times 10^{-7}$  and unperturbed equilibrium orbits to accumulate the power transfer for each  $\delta f$  marker in the phase space hypercube. The results are presented in figure 10 as functions of invariants  $E$ ,  $\Lambda \equiv \mu B_0/E$ , and  $P_\phi$ . Although the whole hypercube is populated in the simulation, only a selection of markers with appreciable power transfer is shown to assist with visualising the key features. A strong resonance can be identified clearly in the range 300–600 keV with a faint sideband at around

200 keV. Analysis of the orbital periods for the resonant particles shows that the strongest power transfer occurs at the precessional resonance  $p = 0$  in equation (5) with the weaker line corresponding to  $p = 1$ . The finding that the TAE is destabilized exclusively by particles in the hundreds of keV range can be readily compared with the distribution function produced by ICRH modelling in figure 5. It appears likely that a large uncertainty in the poorly resolved tail of the ICRH minority distribution is responsible for the large computed drive. Noisy neutral particle analyser (NPA) measurements taken during the afterglow imply a lost minority hydrogen tail temperature in the range 170–220 keV. Again, uncertainty propagation in the ICRH distribution functions appears crucial to raise linear drive calculations to the point of falsifiability.

### 3.7. Breakdown of analytical Landau damping theory in JET limit

The difference is striking between the analytical estimate of ion Landau damping and the linear computation in three different models—drift-kinetic, gyrokinetic and full-orbit. The idealised expression given by equation (10) includes only deeply passing particle resonances, and only includes the lowest order bounce harmonics  $v_{\parallel} = V_A$  and  $v_{\parallel} = V_A/3$ . Both these approximations are very significant under these conditions when examining the power transfer in figure 11. Most of the markers are where non-resonant random power transfer occurs. Poloidal flux in our convention is positive and small at the magnetic axis, and positive and large at the plasma edge, indicating that low values of  $P_\phi = Ze\psi + O(\frac{r}{L})$  are near the bottom of figure 11. Furthermore, co-passing particles travel in the negative  $\phi$  direction on JET, meaning that fast co-passing particles are found at the very bottom of the figure. For particles at low  $\Lambda$ , the particles are passing, and a thin surface corresponding to  $P_\phi = mRv_\phi + Ze\psi_{\text{TAE}}$  is traced, owing to the TAE peaking at one value of poloidal flux  $\psi_{\text{TAE}}$ , and this radial position must be encountered by the particle over its orbit to perform appreciable work on the mode. The energies associated with a passing particle resonance condition are 585 keV, 65 keV, 23 keV and 12 keV corresponding to  $V_A$ ,  $\frac{V_A}{3}$ ,  $\frac{V_A}{5}$ ,  $\frac{V_A}{7}$  respectively. Unsurprisingly, the  $V_A$  plays no role for a thermal plasma at tens of keV, however perhaps more surprising is that  $\frac{V_A}{3}$  does not contribute either. It is found that the  $\frac{V_A}{5}$ ,  $\frac{V_A}{7}$  lines are actually the main passing particle resonances, with  $\frac{V_A}{5}$  the most important at these temperatures. Therefore, a large missing term resembling  $g(\frac{\lambda}{5})$  in equation (10) appears to be appropriate for JET like conditions, and explains much of the discrepancy with the analytical theory of ion Landau damping. This suggests at least a factor 10 under-estimate of ion Landau damping in some previous analytical JET work [37]. Connor *et al* [9] anticipated that because of ellipticity and Shafranov shift, the work done by passing particles  $v_D \cdot \delta E$ , when integrated over an orbit, contains small amounts of poloidal harmonics such as  $k_{\parallel} = 5/2qR$  and  $k_{\parallel} = 7/2qR$  corresponding to  $\frac{V_A}{5}$ ,  $\frac{V_A}{7}$ . They concluded that a better approximation to ion

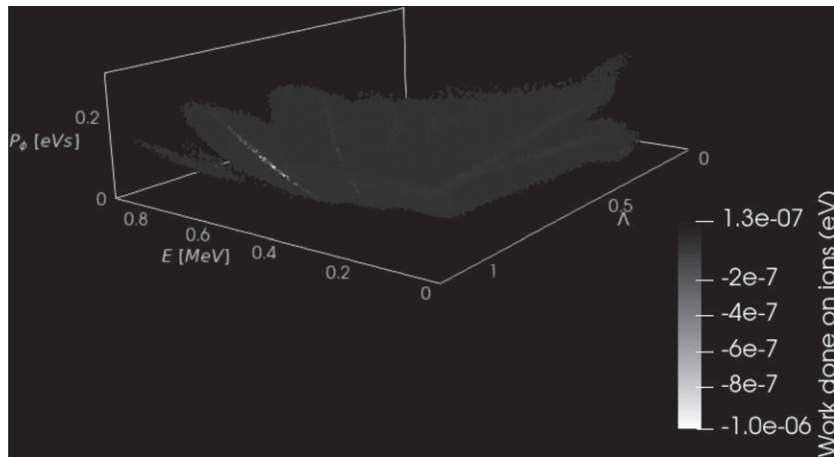


**Figure 10.** HALO computed wave–particle power transfer for particles in phase space between minority ICRH ions and the  $n = 5$  TAE. The  $p = 0$  precessional resonance is most prominent.

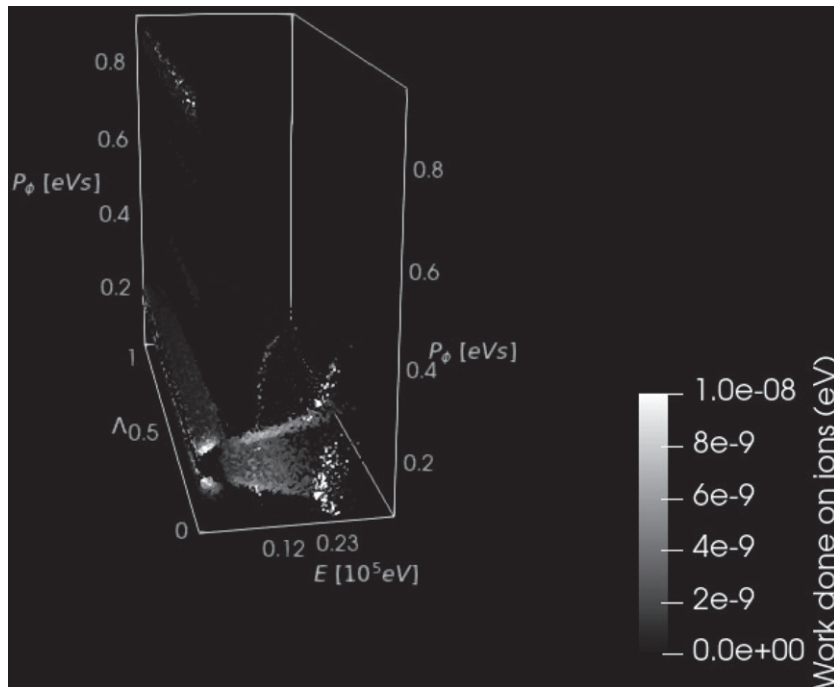


**Figure 11.** HALO computed wave–particle power transfer for particles in phase space. The bright line at 23 kV corresponds to the  $\frac{v_A}{5}$  sideband TAE resonance condition.

Landau damping is given by

$$\frac{\gamma}{\omega} = -q^2\beta \left[ g\left(\frac{\lambda}{3}\right) + \left[ \frac{3}{4}\Delta' + \frac{3E}{4r} - \frac{5E'}{4} \right]^2 g\left(\frac{\lambda}{5}\right) + \left[ \frac{7}{12}E' - \frac{3E}{4r} \right]^2 g\left(\frac{\lambda}{7}\right) \right] \quad (11)$$

with  $\Delta(r)$  the equilibrium Shafranov shift,  $E/r = (\kappa - 1)/(\kappa + 1)$  the ellipticity parameter, and dash denotes radial gradient. However, we have not verified that ellipticity and Shafranov shift are the main causes for the sideband resonance in this case and no clear account is made for trapped particles, which are calculated to be dominant by CASTOR-K (a

result not replicated by HALO or LIGKA). The accuracy of this more detailed expression should be investigated in more detail in future work.

As has been noted previously [38], both co and counter passing particles resonate with the TAE owing to the pair of poloidal harmonics travelling opposite poloidal directions, so the  $\frac{v_A}{5}$  resonance can be observed on both co and counter passing branches of  $P_\phi \approx Ze\psi_{\text{TAE}}$  in figure 11.

### 3.8. Extrapolated kinetic alpha equilibrium from 96852 to DT

Having identified that the majority of the damping for the observed core TAEs occurs because of radiative damping, a finite plasma temperature effect, we extrapolate the conditions



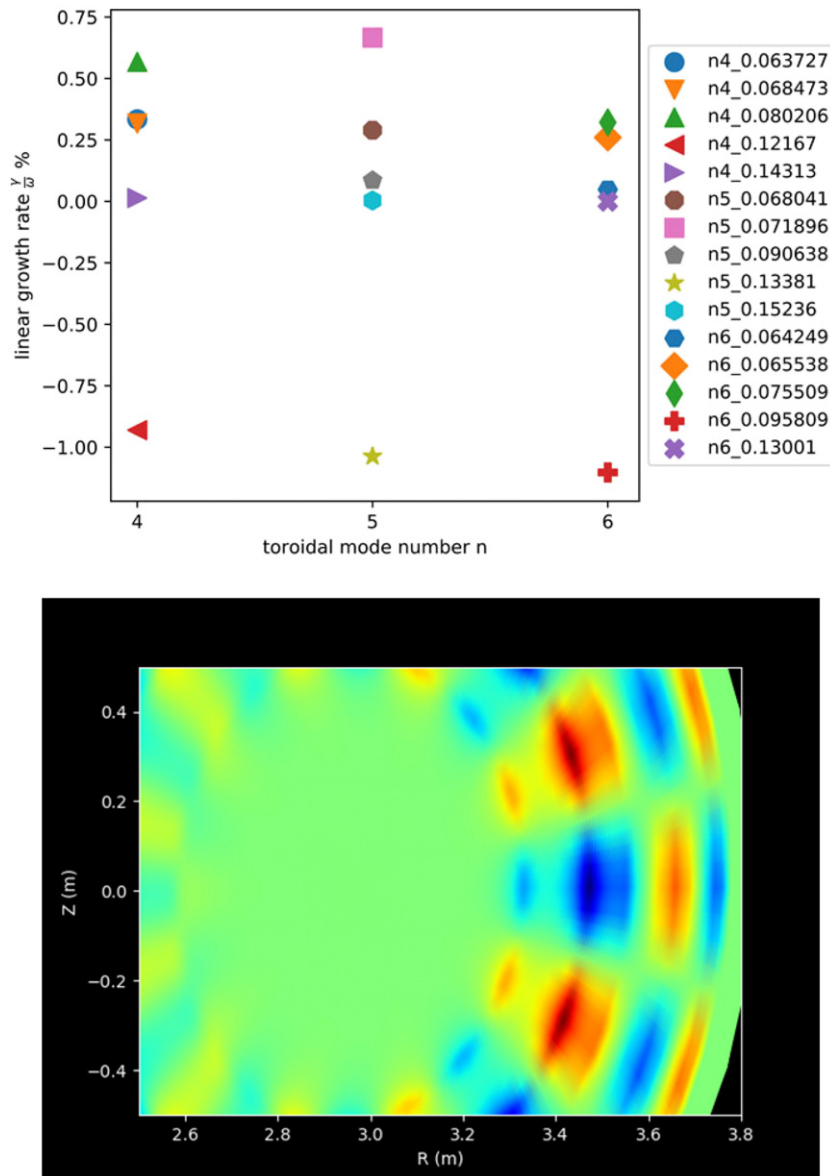


**Figure 12.** HALO alpha drive calculations for the eigenmodes from 92416 using the alpha pressure predicted for 96852 (above) and strongest alpha driven 146 kHz  $n = 5$  mode (below).

of our DD scenario to DT to predict whether these modes can be driven by alpha particles late in the afterglow when the core ion temperature has decreased. A standard DT extrapolation method for JET is to perform interpretive modelling using the TRANSP code to obtain good agreement for predicted fusion rates and stored energy, then to re-run the interpretive case assuming a DT gas mixture. No thermal transport is modelled and only experimental profiles are used in the extrapolation. A number of similar afterglow experiments with small variations in fuelling and NBI timing were conducted in the absence of ICRH, the best performing in DD was shot 96852. This was chosen as the basis for fusion power extrapolation. The aim of this extrapolation is to examine the feasibility of driving similar TAEs when alpha particles are providing the drive instead of ICRH minority ions, assuming the best performing ITB scenarios in DD can be re-established in DT.

To obtain a smooth alpha distribution function, an isotropic slowing down distribution [39] was assumed of the form

$$\begin{aligned}
 F(E [\text{eV}], \mu [\text{eV T}^{-1}], P_\phi [\text{J s}]) &= n(\psi(E, \mu, P_\phi)) \frac{N}{v^3 + v_c^3} \text{Erfc} \left[ \frac{E - 3.5 \times 10^6 \text{ eV}}{106 \times 10^3 \sqrt{T_{i0} [\text{keV}]}} \right] \\
 v_c &\equiv \left( 3\sqrt{\pi} \frac{m_e Z_1}{4} \right)^{\frac{1}{3}} \sqrt{\frac{2T_{e0}}{m_e}} \\
 Z_1 &= \frac{0.5}{2m_p} + \frac{0.5}{3m_p} \\
 Ze\psi(E [\text{eV}], \mu [\text{eV T}^{-1}], P_\phi [\text{J s}]) &\approx P_\phi - mR_0 \sqrt{2(E - \mu B_0)/m} \quad (12)
 \end{aligned}$$

where the alpha density profile prediction  $n(\psi)$  was taken from signal NFI from TRANSP using the lowest order approximation to the orbit-average poloidal flux, and only the on-axis

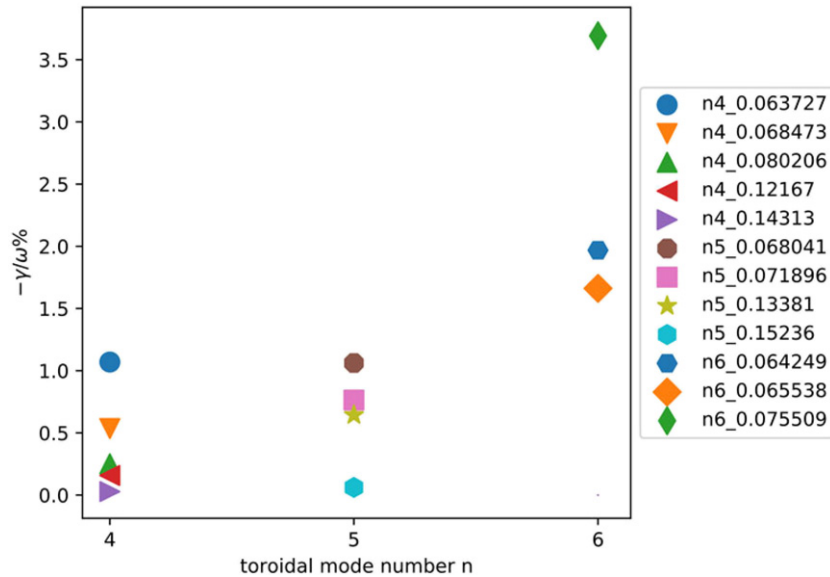


Figure 13. CASTOR radiative damping calculations for the MISHKA-1 identified modes.

temperature was used to avoid the complication of a spatial dependence in the normalization factor  $N$ .

### 3.9. DT predictions

Linear alpha drive calculations for the beginning of the afterglow were performed using the assumed slowing down form of the TRANSP alpha distribution function for the extrapolation of 96852. This corresponds to achieving a fusion power in DT of  $P_{\text{fus}} = 8.5$  MW with the ITB afterglow scenario. The result of the HALO calculation assuming the same eigenmodes as found for 92416 is presented in figure 12. The modes that are most driven by alpha particles are still somewhat in the core region, although not to the extent seen with ICRH drive. It is likely that the broadness of the assumed alpha distribution changes the position of the radial gradient maximum. Radial drive occurs when the fast ion diamagnetic frequency  $n\omega_*$  at resonance exceeds the mode frequency  $\omega$  where

$$\omega_* \equiv \left( \frac{\partial F}{\partial P_\phi} \right)_{E,\mu} / \left( \frac{\partial F}{\partial E} \right)_{\mu,P_\phi}$$

as expressed by equation (6). The larger orbit widths and Larmor radii of alpha particles would also favour broader modes found at lower toroidal mode number and radial position than those driven by ICRH. The maximum drive obtained was  $\frac{\gamma_L}{\omega} = 0.75\%$  which is approximately a factor of 5 lower than the damping found for DD before the afterglow.

These values of alpha drive can be compared with the radiative damping at the end of the afterglow. The complex resistivity procedure was repeated for all the MISHKA-1 obtained ideal eigenmodes assuming a 50:50 DT plasma, although not all eigenmodes could be re-obtained with the complex resistivity calculation due to a reduced set of poloidal harmonics used in the more computationally demanding CASTOR calculations. The results of the radiative damping for all modes at the end of the DT afterglow are presented figure 13. Subtracting the radiative damping in figure 13 from the alpha drive in

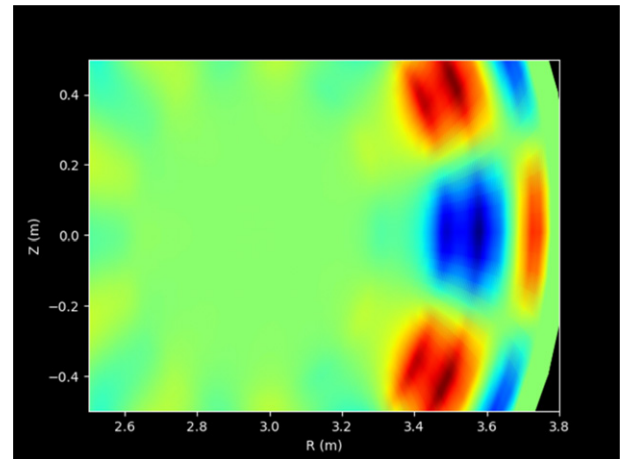


Figure 14. 142 kHz  $n = 4$  eigenmode with strongest net drive i.e.: alpha drive implied by 96852 minus radiative damping from 92416.

figure 12, we find that almost all the modes are stable, with the radiative damping swamping the alpha drive even for 8.5 MW of fusion power.

This requirement that the confined alpha power exceed  $P_\alpha \approx 2$  MW for marginal TAE instability can be compared with the  $P_{\text{ICRH}} = 4.5$  MW required to produce three marginally unstable core TAEs during the afterglow in shot 92416. The sole unstable alpha driven mode predicted is an  $n = 4$  eigenmode at 142 kHz in the lab frame, found closer to the edge of the plasma (figure 14).

## 4. Conclusion

Detailed calculations of TAE stability during the JET ITB afterglow were performed using the best available data on the thermal and kinetic equilibrium. EFIT reconstructions using TRANSP fast pressure and measured thermal profiles together with low order representation for the flux functions

gave good agreement with  $q$ -profiles obtained via MHD spectroscopy in these scenarios. Subsequent incompressible MHD calculations on this equilibrium predicted both the frequency and position of modes observed. Perturbative calculations of ICRH drive and NBI damping were conducted using manual fits to Monte-Carlo data, leading to a gross overprediction of ICRH drive given that mode destabilization occurred later than predicted. The majority of computed ICRH drive came from the toroidal precessional resonance where ICRH distributions were poorly resolved. However, the modes predicted to experience the strongest drive are those observed in experiment, and modes predicted to be driven the least are not observed at all.

Non-perturbative calculations with CASTOR and LIGKA confirm that the Maxwellian bulk plasma is responsible for strong radiative damping of core modes contributing roughly half the damping during the high-performance phase of DD experiments, the other half coming from than the NBI ions. The total damping was calculated to be of the order of  $\frac{\gamma}{\omega} = 4\%$  at its peak. Analytical Landau damping estimates in JET-like conditions require contribution from  $V_A/5$  sideband resonance to avoid underprediction, although even then, the Landau damping was found to be small. DT extrapolations giving  $P_{\text{fus}} = 8.5$  MW indicate marginal instability of an  $n = 4$  TAE outside the core, with all other TAEs for  $n = 4, 5, 6$  found to either be suppressed by the radiative damping, or too high frequency to be driven by the radial gradient.

We anticipate that a likely follow-up study to this work will compute all known linear drive and damping contributions for every mode identified in linear and nonlinear regimes, as has been performed previously for ITER (e.g.: [31, 32, 40]). In this work, we have instead focussed on the validity of reduced models to capture the essential measurable features in order to improve the credibility of such comprehensive predictions. Certainly, this work should be revisited when alpha particles are present and uncertainties in inputs to stability calculations are reduced. We should demand greater fidelity in our predictive capability in order to be of assistance to those making design decisions for future reactors. We should also explore large-scale uncertainty quantification techniques, propagating all the errors in the equilibrium distributions, leading to actionable predictions and more clarity on theory shortcomings.

The finding that radiative damping is a dominant factor in the stability of core TAEs should be considered good news for fast ion confinement in burning plasma, even if it poses a significant challenge to overcome for driving TAEs with alphas in JET DT.

## Acknowledgments

The first author is indebted to Philipp Lauber and Andreas Bierwage for providing LIGKA calculations on short notice. This work has been carried out within the framework of the EUROfusion Consortium and has received funding from the Euratom Research and Training Programme 2014–2018 and 2019–2020 under Grant Agreement No. 633053 and from the RCUK Energy Programme (Grant Number EP/P012450/1).

The views and opinions expressed herein do not necessarily reflect those of the European Commission. To obtain further information on the data and models underlying this paper please contact [PublicationsManager@ukaea.uk](mailto:PublicationsManager@ukaea.uk).

## ORCID iDs

S.E. Sharapov <https://orcid.org/0000-0001-7006-4876>  
 E. Tholerus <https://orcid.org/0000-0002-3262-1958>  
 M. Dreval <https://orcid.org/0000-0003-0482-0981>  
 P. Vallejos <https://orcid.org/0000-0003-4343-6325>  
 T. Johnson <https://orcid.org/0000-0002-7142-7103>  
 P. Rodrigues <https://orcid.org/0000-0001-6189-6865>  
 A. Figueiredo <https://orcid.org/0000-0003-0487-8956>  
 F. Nabais <https://orcid.org/0000-0003-4644-2827>  
 R. Dumont <https://orcid.org/0000-0002-1030-138X>

## References

- [1] Fasoli A. *et al* 2007 Progress in the ITER physics basis chapter 5: physics of energetic ions *Nucl. Fusion* **47** S264–84
- [2] Dumont R.J. *et al* 2018 Scenario development for the observation of alpha-driven instabilities in JET DT plasmas *Nucl. Fusion* **58** 082005
- [3] Sharapov S.E., Borba D., Fasoli A., Kerner W., Eriksson L.-G., Heeter R.F., Huysmans G.T.A. and Mantsinen M.J. 1999 Stability of alpha particle driven Alfvén eigenmodes in high performance JET DT plasmas *Nucl. Fusion* **39** 373–88
- [4] Nazikian R. *et al* 1997 Alpha-particle-driven toroidal Alfvén eigenmodes in the tokamak fusion test reactor *Phys. Rev. Lett.* **78** 2976–9
- [5] Sauter O. and Medvedev S.Y. 2013 Tokamak coordinate conventions: COCOS *Comput. Phys. Commun.* **184** 293–302
- [6] Cooper W. and Wootton A. 1982  $\beta_p$  analysis for tokamak plasma with anisotropic pressure and mass flow *Plasma Phys.* **24** 1183
- [7] Cheng C.Z. and Chance M.S. 1986 Low- $n$  shear Alfvén spectra in axisymmetric toroidal plasmas *Phys. Fluids* **29** 3695
- [8] Candy J. and Rosenbluth M.N. 1994 Nonideal theory of toroidal Alfvén eigenmodes *Phys. Plasmas* **1** 356–72
- [9] Connor J.W., Dendy R.O., Hastie R.J., Borba D., Huysmans G., Kerner W. and Sharapov S. 1994 Non-ideal effects on toroidal Alfvén eigenmode stability *21st EPS Conf. on Controlled Fusion and Plasma Physics* (Montpellier, France, 27 Jun–1 Jul 1994) ([http://libero.ipp.mpg.de/libero/PDF/EPS\\_21\\_Vol2\\_1994.pdf](http://libero.ipp.mpg.de/libero/PDF/EPS_21_Vol2_1994.pdf))
- [10] Borba D. and Kerner W. 1999 CASTOR-K: stability analysis of Alfvén eigenmodes in the presence of energetic ions in tokamaks *J. Comput. Phys.* **153** 101–38
- [11] Gorelenkov N.N., Cheng C.Z. and Fu G.Y. 1999 Fast particle finite orbit width and Larmor radius effects on low- $n$  toroidicity induced Alfvén eigenmode excitation *Phys. Plasmas* **6** 2802–7
- [12] Pinches S.D. *et al* 1998 The HAGIS self-consistent nonlinear wave-particle interaction model *Comput. Phys. Commun.* **111** 133–49
- [13] Fitzgerald M., Buchanan J., Akers R.J., Breizman B.N. and Sharapov S.E. 2020 HALO: a full-orbit model of nonlinear interaction of fast particles with eigenmodes *Comput. Phys. Commun.* **252** 106773
- [14] Mikhailovskii A.B., Huysmans G.T.A., Kerner W.O.K. and Sharapov S.E. 1997 Optimization of computational MHD

- normal-mode analysis for tokamaks *Plasma Phys. Rep.* **23** 844–57
- [15] Kerner W., Goedbloed J.P., Huysmans G.T.A., Poedts S. and Schwarz E. 1998 CASTOR: normal-mode analysis of resistive MHD plasmas *J. Comput. Phys.* **142** 271–303
- [16] Nyqvist R.M. and Sharapov S.E. 2012 Asymmetric radiative damping of low shear toroidal Alfvén eigenmodes *Phys. Plasmas* **19** 082517
- [17] Könies A. *et al* 2018 Benchmark of gyrokinetic, kinetic MHD and gyrofluid codes for the linear calculation of fast particle driven TAE dynamics *Nucl. Fusion* **58** 126027
- [18] Spong D.A. *et al* 2012 Verification and validation of linear gyrokinetic simulation of Alfvén eigenmodes in the DIII-D tokamak *Phys. Plasmas* **19** 082511
- [19] Lauber P., Günter S., Könies A. and Pinches S.D. 2007 LIGKA: a linear gyrokinetic code for the description of background kinetic and fast particle effects on the MHD stability in tokamaks *J. Comput. Phys.* **226** 447–65
- [20] Porcelli F., Stankiewicz R., Kerner W. and Berk H.L. 1994 Solution of the drift-kinetic equation for global plasma modes and finite particle orbit widths *Phys. Plasmas* **1** 470–80
- [21] Betti R. and Freidberg J.P. 1992 Stability of Alfvén gap modes in burning plasmas *Phys. Fluids B* **4** 1465–74
- [22] Sharapov S.E. *et al* 2008 Chapter 5: burning plasma studies at JET *Fusion Sci. Technol.* **53** 989–1022
- [23] Nabais F. *et al* 2018 TAE stability calculations compared to TAE antenna results in JET *Nucl. Fusion* **58** 082007
- [24] Brix M., Hawkes N.C., Boboc A., Drozdov V. and Sharapov S.E. 2008 Accuracy of EFIT equilibrium reconstruction with internal diagnostic information at JET *Rev. Sci. Instrum.* **79** 10F325
- [25] Svensson J. and Werner A. (JET-EFDA Contributors) 2008 Current tomography for axisymmetric plasmas *Plasma Phys. Control. Fusion* **50** 085002
- [26] Hawryluk R J 1979 An empirical approach to tokamak transport *Physics of Plasmas Close to Thermonuclear Conditions* (Varenna, Italy: CEC, Brussels)
- [27] Baruzzo M. *et al* 2010 Neoclassical tearing mode (NTM) magnetic spectrum and magnetic coupling in JET tokamak *Plasma Phys. Control. Fusion* **52** 075001
- [28] Joffrin E. *et al* 2003 Internal transport barrier triggering by rational magnetic flux surfaces in tokamaks *Nucl. Fusion* **43** 1167–74
- [29] Huysmans G.T.A., Goedbloed J.P. and Kerner W. 1991 Isoparametric bicubic hermite elements for solution of the Grad–Shafranov equation *Int. J. Mod. Phys. C* **02** 371–6
- [30] Berk H.L., Van Dam J.W., Borba D., Candy J., Huysmans G.T.A. and Sharapov S. 1995 More on core-localized toroidal Alfvén eigenmodes *Phys. Plasmas* **2** 3401–6
- [31] Fitzgerald M., Sharapov S.E., Rodrigues P. and Borba D. 2016 Predictive nonlinear studies of TAE-induced alpha-particle transport in the  $Q = 10$  ITER baseline scenario *Nucl. Fusion* **56** 112010
- [32] Rodrigues P., Figueiredo A., Ferreira J., Coelho R., Nabais F., Borba D., Loureiro N.F., Oliver H.J.C. and Sharapov S.E. 2015 Systematic linear-stability assessment of Alfvén eigenmodes in the presence of fusion  $\alpha$ -particles for ITER-like equilibria *Nucl. Fusion* **55** 083003
- [33] Hedin J., Hellsten T., Eriksson L.-G. and Johnson T. 2002 The influence of finite drift orbit width on ICRF heating in toroidal plasmas *Nucl. Fusion* **42** 527–40
- [34] Hirvijoki E., Asunta O., Koskela T., Kurki-Suonio T., Miettunen J., Sipilä S., Snicker A. and Äkäslompolo S. 2014 ASCOT: solving the kinetic equation of minority particle species in tokamak plasmas *Comput. Phys. Commun.* **185** 1310–21
- [35] Di Troia C. 2012 From the orbit theory to a guiding center parametric equilibrium distribution function *Plasma Phys. Control. Fusion* **54** 105017
- [36] Di Troia C. 2015 Bayesian derivation of plasma equilibrium distribution function for tokamak scenarios and the associated Landau collision operator *Nucl. Fusion* **55** 123018
- [37] Seo J. *et al* 2020 Parametric study of linear stability of toroidal Alfvén eigenmode in JET and KSTAR *Nucl. Fusion* **60** 066008
- [38] Todo Y. and Sato T. 1998 Linear and nonlinear particle-magnetohydrodynamic simulations of the toroidal Alfvén eigenmode *Phys. Plasmas* **5** 1321
- [39] Gaffey J.D. 1976 Energetic ion distribution resulting from neutral beam injection in tokamaks *J. Plasma Phys.* **16** 149
- [40] Figueiredo A.C.A. *et al* 2016 Comprehensive evaluation of the linear stability of Alfvén eigenmodes driven by alpha particles in an ITER baseline scenario *Nucl. Fusion* **56** 076007